ARTICLE

Electrochemically reconfigurable architected materials

Xiaoxing Xia[1], Arman Afshar[2], Heng Yang[1], Carlos M. Portela[1], Dennis M. Kochmann[1,3], Claudio V. Di Leo[2] & Julia R. Greer[1]*

Architected materials can actively respond to external stimuli—such as mechanical forces, hydration and magnetic fields—by changing their geometries and thereby achieve novel functionalities. Such transformations are usually binary and volatile because they toggle between 'on' and 'off' states and require persistent external stimuli. Here we develop three-dimensional silicon-coated tetragonal microlattices that transform into sinusoidal patterns via cooperative beam buckling in response to an electrochemically driven silicon-lithium alloying reaction. In situ microscopy reveals a controllable, non-volatile and reversible structural transformation that forms multiple ordered buckling domains separated by distorted domain boundaries. We investigate the mechanical dynamics of individual buckling beams, cooperative coupling among neighbouring beams, and lithiation-rate-dependent distributions of domain sizes through chemo-mechanical modelling and statistical mechanics analysis. Our results highlight the critical role of defects and energy fluctuations in the dynamic response of architected materials. We further demonstrate that domain boundaries can be programmed to form particular patterns by pre-designing artificial defects, and that a variety of reconfigurational degrees of freedom can be achieved through micro-architecture design. This framework enables the design, fabrication, modelling, behaviour prediction and programming of electrochemically reconfigurable architected materials, and could open the way to beyond-intercalation battery electrodes, tunable phononic crystals and bio-implantable devices.

Architected materials represent an area of active research because they exhibit exotic properties such as negative Poisson's ratios[1,2] and negative refractive indices[3,4], and decouple historically correlated material properties such as strength versus density[5,6] and thermal conductivity versus stiffness[7]. Most architected materials reported to date are passive in the sense that they have a prescribed geometry fulfilling a single functionality. It was recently shown that architected materials can be reconfigured by mechanical deformation[8] and instabilities[9–12], hydration-induced swelling[13–16] and magnetic actuation[17]. Such smart, stimulus-responsive materials can make a long-lasting impact on adaptive, deployable and dynamically tunable devices if they could overcome existing challenges of (1) requiring bulky external control, (2) toggling between 'on' and 'off' states, and (3) reverting to the original configuration once external stimulus is removed. Most of these reconfigurable systems are small and idealized; scaling them up requires substantially increasing the number of repeating units that would inevitably introduce inhomogeneities[18,19] similar to defects, gradients or grain boundaries that govern the properties of classical materials[20]. Here we demonstrate a new mechanism to dynamically reconfigure architected materials by exploiting electrochemically driven alloying/dealloying reactions to induce continuous, non-volatile and reversible structural transformations. We use the alloying couple of silicon (Si) and lithium (Li) as a prototype system because Si is a high-capacity battery electrode material notorious for its approximately 300% volumetric expansion after full lithiation[21]. We investigate the cooperation between buckling instabilities in architected materials that transform into ordered buckling domains separated by distorted domain boundaries. Buckling has been observed in Si nanowires[22] and etched honeycomb patterns[23,24] during lithiation, but it has not been systematically studied as a design tool to achieve architectural reconfiguration.

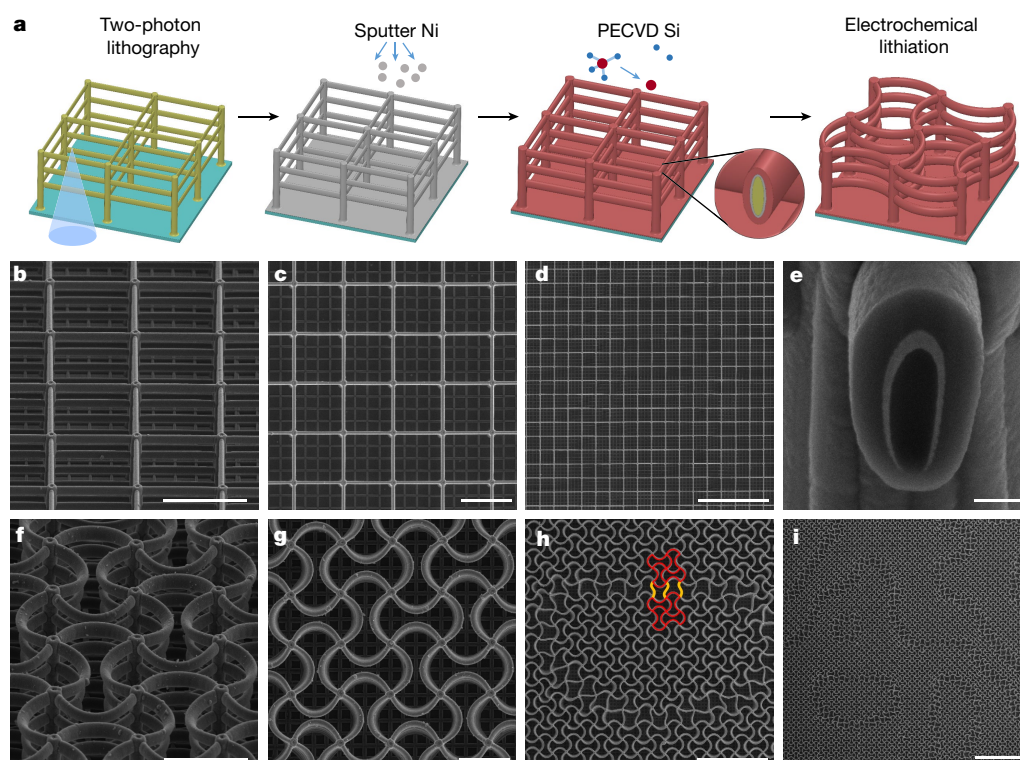## Fabrication and lithiation of Si microlattices

To create micro-architectures with a propensity for collective in-plane buckling, we designed a periodic three-dimensional (3D) tetragonal lattice with slender horizontal beams connected to stubby vertical posts. Figure 1a shows a schematic of this geometry and the fabrication process (see Methods and Supplementary Information section I). We first printed a polymer lattice using two-photon lithography, then sputtered an approximately 100-nm-thick Ni layer and deposited an amorphous Si layer about 300 nm thick onto each beam using plasma-enhanced chemical vapour deposition (PECVD). Each sample contained 79 (width) × 79 (length) × 5 (height) unit cells, and each tetragonal unit cell had a width of 20 μm and a height of 5 μm (Fig. 1b–e). Horizontal beams had an elliptical cross-section with a vertical major axis of about 2.6 μm and a minor axis of about 1.3 μm; vertical posts had a circular cross-section with a diameter of approximately 2.6 μm. A square grid with 5-μm spacing was patterned on the substrate to prevent delamination of Si film underneath the microlattice (Fig. 1c). Each sample contained about 8.0 μg of Si as the electrochemically active component, with an areal Si loading of 0.25 mg cm^{-2}.

Lithiation of Si microlattices was conducted galvanostatically at a constant current of 5 μA with a Li counter electrode until the voltage dropped to a cutoff voltage of 0.01 V versus Li/Li$^+$ (see Methods and Supplementary Information section II). This current corresponds to a current density of 0.15 mA cm^{-2} and a C-rate of about C/6 (a C-rate of 1C represents the current at which it takes 1 h to attain the theoretical capacity of the electrode, which is 3,600 mAh per g Si)[25]. Under these conditions, an average of about 80% of the theoretical capacity was attained after the first lithiation, which corresponds to an approximately 240% volumetric expansion in the Si shell[26]. Scanning electron microscopy (SEM) images in Fig. 1f–i demonstrate that Si microlattices deformed via cooperative beam buckling to create an orthogonal sinusoidal pattern with pairwise opposite concavity upon lithiation. Each horizontal beam accommodated the volumetric expansion through radial growth of cross-sectional area and axial elongation in length, which prompted in-plane buckling. Each pair of nearest-neighbour nodes rotated in opposite directions in response to buckling-induced

Fig. 1 | Fabrication process and SEM characterization of Si microlattices before and after lithiation. a, Illustration of the fabrication process for Si microlattices and their structural transformation after lithiation. **b–d**, SEM images of as-fabricated Si microlattices at different magnifications and tilts. **e**, SEM image of a cross-section of a representative horizontal polymer-Ni-Si beam, milled by a focused ion beam, that shows a slight variation in the Ni and Si layer thickness. **f–i**, SEM images of Si microlattices lithiated at a current of C/6 with a cutoff voltage of 0.01 V. Panels **f** and **g** show the orthogonal sinusoidal pattern formed via cooperative buckling; **h** and **i** show multiple bistable domains joined at clearly visible boundaries. Panel **h** contains an overlaid illustration of two ordered domains, with mode-I buckled beams (red) connected by mode-II buckled beams (yellow) at the domain boundary. Orientation details: **b**, **e** and **f** are at a 52° tilt angle; **c**, **d**, **g**, **i**, **j** are top-down views. Scale bars: **b**, **c**, **f**, **g**, 20 μm; **d**, **h**, 100 μm; **e**, 500 nm; and **i**, 200 μm.

torque. We did not observe any cracking in the beams after lithiation, and the lattice remained in this stable, buckled state after removing the applied current. The buckling directions of four horizontal beams connected at a specific node were coupled through the node's rotation, and such cooperative buckling led to the formation of the ordered sinusoidal patterns (Fig. 1g), within which each beam constituted half the wavelength via mode-I buckling (labelled in red in Fig. 1h). The bistability of in-plane beam buckling led to the formation of multiple ordered domains mismatched by one unit cell (Fig. 1h, i); beams at the domain boundaries deformed via mode-II buckling with a mid-span change of concavity (labelled in yellow in Fig. 1h). The buckling pattern was identical across all out-of-plane layers because of the twisting of the vertical posts (Fig. 1f). Such lithiation-induced cooperative buckling is not specific to this Si-Li chemistry. Sn microlattices fabricated by sputtering Sn directly onto the polymer scaffold exhibited similar cooperative buckling upon lithiation (Extended Data Fig. 1 and Supplementary Information section V).

Reversibility of lithiation–induced buckling

We constructed an in situ optical set-up to capture the dynamics of cooperative buckling and domain formation. A custom-made electrochemical cell with a quartz window was used to visualize structural transformations at a constant current of C/6 under a digital optical microscope (Extended Data Fig. 2b, c and Supplementary Information section III). Real-time snapshots of a typical in situ experiment at progressively lower voltages during lithiation are shown in Fig. 2a, and those at progressively higher voltages during delithiation are shown in Fig. 2b. Lithiation and delithiation were conducted until cutoff voltages of 0.01 V and 1.5 V, respectively. An in situ lithiation video (Supplementary Video 1) reveals that initial buckling occurred rapidly in all horizontal beams, which continued to buckle more gradually

as lithiation proceeded. Domain boundaries emerged spontaneously between mismatched domains. During delithiation, the horizontal beams almost fully unbuckled, and multiple nodes fractured when voltage increased above about 0.6 V (Supplementary Video 2). The Si-Li alloying reaction is a spontaneous discharge process, which implies that lithiation-induced cooperative buckling does not require an external energy supply. Supplementary Video 3 presents thermodynamically driven lithiation and buckling of a Si microlattice when a 2,000 Ω resistor was connected to the in situ cell, drawing current from the alloying reaction. Supplementary Video 4 presents lithiation and delithiation cycling at high rates (Supplementary Information section III), where substantial buckling/unbuckling deformations were induced in less than 10 min.

A cyclic voltammogram of the first three cycles (Fig. 2e) shows the reversible Si-Li alloying and dealloying reactions, indicated[27,28] by the reduction peaks around 0.03 V and 0.21 V and the oxidation peaks around 0.33 V and 0.49 V. Noticeable current fluctuations occurred during the third delithiation around 0.55 V, which correlates with local fracture events observed around 0.6 V during in situ delithiation. To investigate if preventing these unstable events could improve cycling reversibility, we conducted galvanostatic cycling tests in coin cells with two delithiation cutoff voltages of 1.5 V and 0.6 V. Figure 2f compares the voltage versus specific capacity profiles of the first and the tenth cycles with these cutoff voltages; voltages that correspond to in situ snapshots in Fig. 2a, b are denoted by yellow symbols. This plot indicates that restricting delithiation voltage to below 0.6 V retained about 30% of the inserted Li during the first lithiation inside the microlattice and substantially improved the reversible capacity of the Si-Li alloying/dealloying reactions. SEM images of Si microlattices after the tenth lithiation and delithiation with 0.6 V delithiation cutoff voltage (Fig. 2c, d) reveal the structural integrity and reversibility of geometric
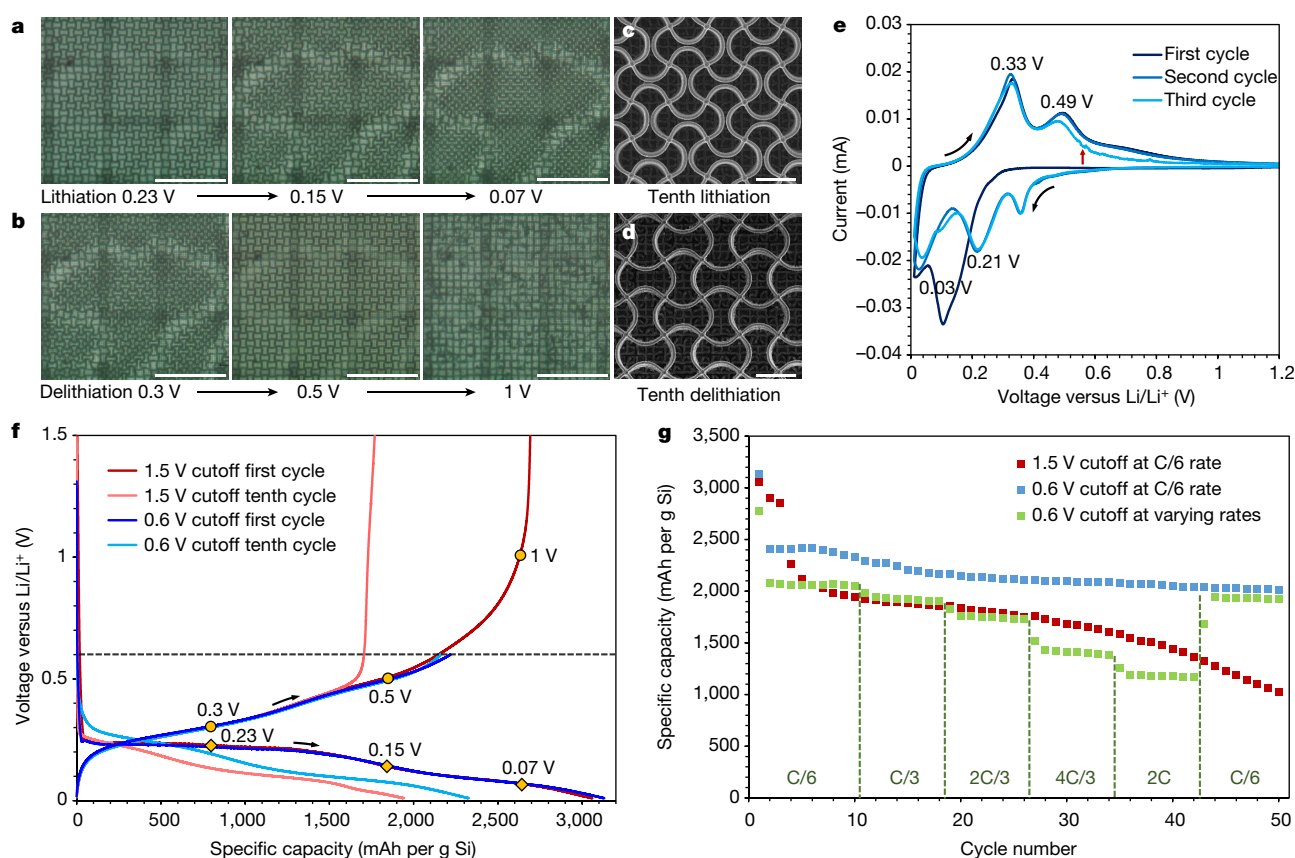
Fig. 2 | In situ optical and electrochemical characterization of lithiation-induced cooperative buckling in Si microlattices. a, b, Progressive optical snapshots during in situ lithiation (**a**) and delithiation (**b**) at different voltages that reveal cooperative buckling, unbuckling and domain formation. **c, d,** SEM images of Si microlattices after the tenth lithiation (**c**) and delithiation (**d**) with 0.6 V delithiation cutoff voltage. **e,** Cyclic voltammogram at a voltage scanning rate of 0.1 mV s^{-1} between 0.01 V and 1.5 V. The red arrow points to emergent current fluctuations around 0.55 V in the third delithiation. **f,** Voltage profiles of the first and the tenth cycles with 1.5 V and 0.6 V delithiation cutoff voltages. Yellow symbols in **f** correspond to voltages shown in **b** and **c** during in situ experiments. **g,** Cycling performance of Si microlattices with 1.5 V and 0.6 V delithiation cutoffs at C/6 and at varying rates up to 2C. Scale bars: **a, b,** 200 μm; **c, d,** 20 μm.

transformations during stable electrochemical cycling. Lithiation capacity versus cycle number plots in Fig. 2g demonstrate stable cycling of Si microlattices; after 50 cycles at C/6, a capacity of 2,010 mAh per g Si was retained for 0.6 V delithiation cutoff compared with that of 1,025 mAh per g Si for 1.5 V delithiation cutoff. Extended cycling performance and analyses are presented in Supplementary Information section IV.

Finite element analysis of individual beams

To investigate the dynamic mechanical behaviour of individual beams during lithiation-induced buckling, we employed a fully-coupled chemo-mechanical continuum finite element analysis (FEA) model[29], which accounts for transient and stress-dependent Li diffusion, large elastic-plastic deformations, and Li-concentration-dependent material properties. Figure 3a shows the simulated mesh on a quarter of a beam (by symmetry, this is extended to the rest of the beam), where the Si elements obey the previously validated constitutive model[29–31], the Ni layer is prescribed an elastic-plastic behaviour, and the polymer core undergoes purely elastic deformation (Supplementary Information section IX). To mimic inevitable fabrication imperfections that cause each beam to deviate from being perfectly straight, we prescribe slightly different ramp rates of incoming Li flux on the two opposite external surfaces of the beam. Supplementary Video 6 summarizes simulation results by showing the dynamic evolution of voltage, geometry and contours of local Li concentration and stresses during lithiation and delithiation. Figure 3a presents progressive snapshots of the beam geometry with normalized Li concentration contours at three different times (t_1, t_2 and t_3). This chemo-mechanical model captures the

lithiation-induced buckling behaviour and predicts a profile of voltage versus state of charge at C/6 comparable to experiments (Fig. 3b); here state of charge is the attained specific capacity normalized by the theoretical capacity. Figure 3c shows contours of σ_{zz} on the mid-span cross-section at t_1, t_2 and t_3, where σ_{zz} is is the stress component normal to the mid-span cross-section; Fig. 3d plots σ_{zz} versus state of charge at three different locations on the mid-span cross-section during lithiation and delithiation. These two plots reveal that during the early stage of lithiation at t_1, the beam elastically buckles with the presence of compressive stresses on the concave side of the buckled beam (point A) and tensile stresses on the convex side (point B). The top of the beam (point C) experiences compressive stresses, which is consistent with the beam having a compressive axial load superimposed with a bending moment due to buckling. With the onset of plastic deformation as lithiation continues, stresses at all three locations become compressive and remain close to the yield stress until lithiation is completed at t_2. During delithiation, the beam contracts and unbuckles to a large degree, resulting in a large tensile stress developing at point A, a lower tensile stress at point C and a slightly compressive stress at point B, all of which increase until the end of delithiation at t_3. The development of large tensile stresses during simulated delithiation correlates well with experimentally observed fracture events at later stages of delithiation (Fig. 2b).

This coupled chemo-mechanical model demonstrates the interplay among different deformation mechanisms during lithiation and provides insights for lattice architecture design. Figure 3e and Supplementary Video 7 compare the effects of four different beam deformation mechanisms on lithiation voltage profiles: (1) straight elastic deformation,
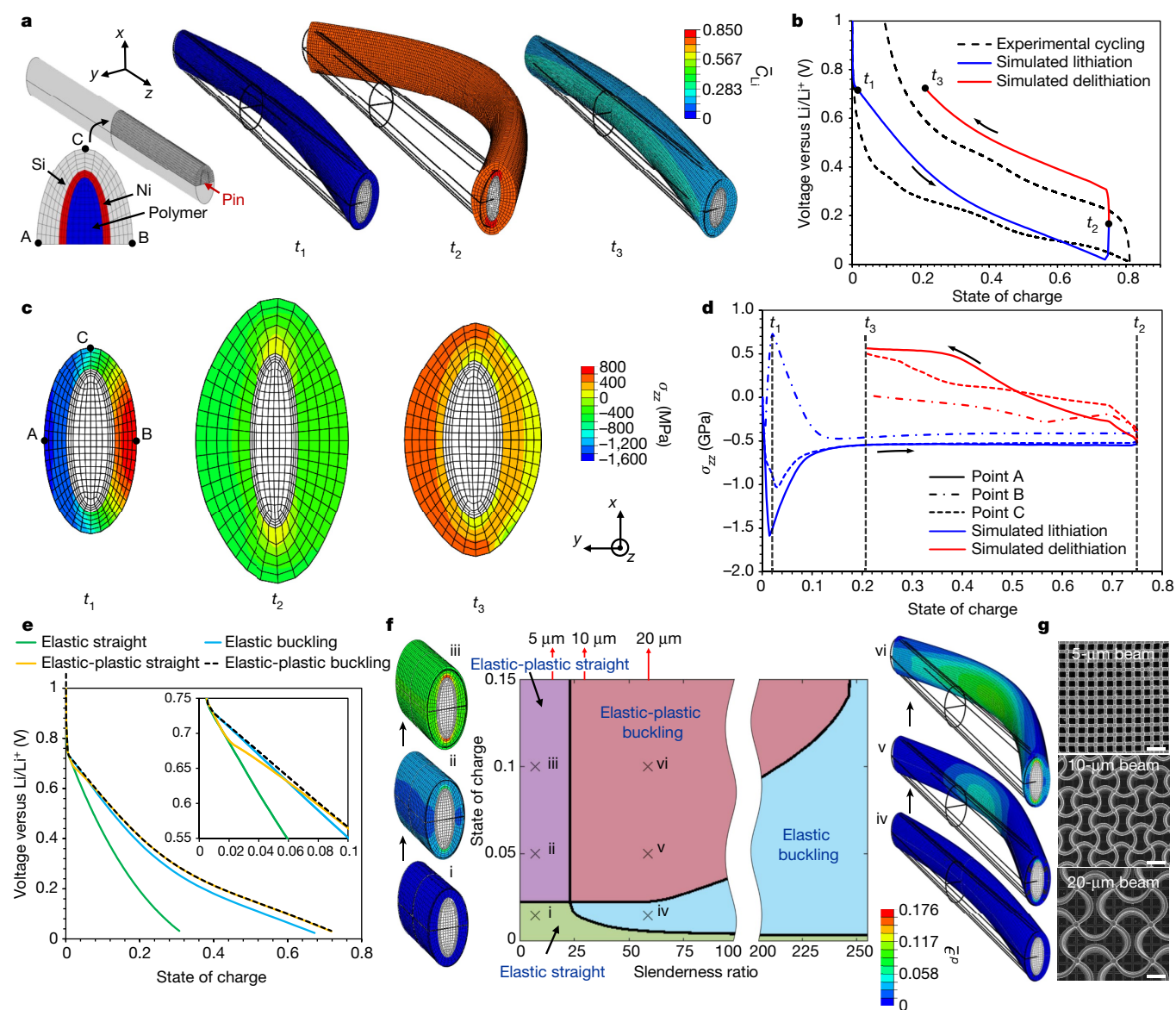
Fig. 3 | Chemo-mechanical FEA modelling of an individual beam. a, 3D mesh of a quarter of a polymer-Ni-Si beam (extended by symmetry to give a whole beam) and simulated beam geometries at different times (t_1, t_2 and t_3) during lithiation and delithiation. Coloured contours represent Li concentration normalized by the maximum possible molar concentration in Li-Si alloys ($\overline{C}_{\mathrm{Li}}$). **b**, Simulated voltage versus state-of-charge profile during lithiation (blue) and delithiation (red) overlaid with an experimental voltage profile from the second cycle with 1.5 V delithiation cutoff voltage at C/6 (dashed black). **c**, σ_{zz} stress colour contours at t_1, t_2 and t_3 on the mid-span cross-section. **d**, σ_{zz} stress versus state-of-charge evolution at points A, B and C (see leftmost panel in **c**) within the mid-span cross-section during lithiation and delithiation. **e**, Voltage versus

state-of-charge profiles of four different beam deformation mechanisms comparing their attainable states of charge at C/10. Inset, zoomed-in plot during the initial stage of lithiation. **f**, Phase map of beam deformation mechanisms as a function of beam slenderness ratio and state of charge obtained from the reduced-order model (main panel), along with FEA-simulated stubby (left) and slender (right) beams with equivalent plastic strain ($\bar{\varepsilon}^p$) coloured contours at different states of charge. i–iii, Progression of lithiation in a stubby beam where buckling does not occur. iv–vi, Progression of lithiation in a slender beam, where elastic buckling precedes plastic deformation. **g**, SEM images of lithiated Si microlattices with different beam lengths of 5 μm, 10 μm and 20 μm. Corresponding beam lengths are labelled on the top axis in **f**. Scale bars: 10 μm.

(2) straight elastic-plastic deformation, (3) purely elastic buckling, and (4) elastic-plastic deformation with buckling. Figure 3e demonstrates that beam-based architectures that allow for buckling, plastic deformation, or a combination of the two could more than double the achievable state of charge at C/10 by reducing stresses during lithiation. Straight elastic-plastic deformation results in a slightly higher voltage than elastic buckling except for the short period before and immediately after the onset of yielding in the beginning of lithiation (Fig. 3e inset). The complete model (elastic-plastic deformation with buckling) predicts a voltage profile that follows the trend of the highest voltage for a given state of charge. This reveals that the interplay among different deformation mechanisms is dynamic, with the most efficient stress relief mechanism governing the voltage profile during different stages of lithiation.

Furthermore, the propensity for buckling instabilities is dictated by the slenderness ratio of a beam (that is, the ratio of its length and its radius of gyration) and contributes to the dominant deformation mechanism at different stages. Figure 3f shows a phase map of beam deformation mechanisms at different slenderness ratios and states of charge predicted by a reduced-order chemo-mechanical model. This model assumes a homogeneous concentration field and a uniaxial stress state, and solves for an elastic beam with pinned boundary conditions undergoing lithiation-induced buckling (Supplementary Information section X). The phase map demonstrates that a stubby beam will first deform elastically and then elastic-plastically without buckling; a slender beam with the same cross-section would first deform elastically and then buckle elastically before yielding (Supplementary Video 8).
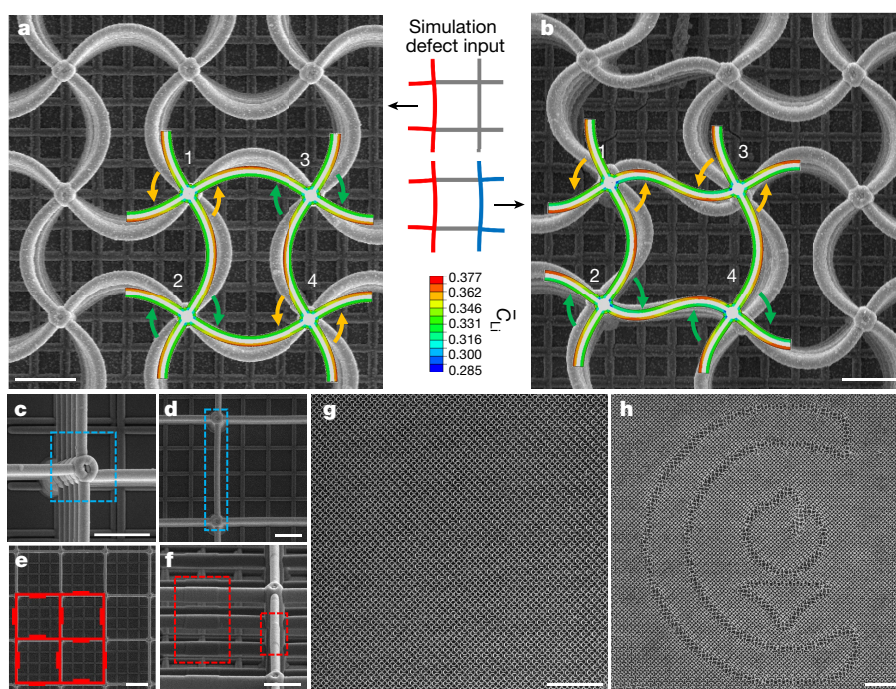
Fig. 4 | Role of defects in domain formation by cooperative buckling.
a, **b**, FEA simulation of a 2D extended unit cell (centre inset) prescribed
with coherent defects (labelled red; **a**) and incompatible defects (labelled
red and blue; **b**) overlaid onto SEM images. Coloured contours represent
normalized Li concentration. **c**–**f**, SEM images of typical defects in Si
microlattices: **c**, stitching misalignment at a node (inside blue box); **d**,
pre-existing beam curvature caused by residual stresses (inside blue

box); and **e**, **f**, periodically arranged artificial defects of 5-μm-long,
100-nm-thick patches on one side of the beams (illustrated in red in **e** and
circled inside red boxes in **f**). **g**, SEM image of a single-domain sinusoidal
lattice formed as a result of defect engineering. **h**, SEM image of a Caltech
icon outlined by domain boundaries that emerged upon lithiation,
produced by pre-designing artificial defects. The Caltech icon is used with
permission. Scale bars: **a**, **b**, **e**, 10 μm; **c**, **d**, **f**, 5 μm; **g**, **h**, 200 μm.

We experimentally corroborated this phase map by fabricating and
lithiating Si microlattices with different beam lengths. SEM images
in Fig. 3g indicate that the transition between straight elastic-plastic
deformation and elastic-plastic buckling occurs between beam lengths
of 5 μm and 10 μm, consistent with the prediction of the reduced-order
model. Adding torsional stiffness to the vertical posts does not quali-
tatively alter the deformation phase map (Supplementary Information
section X).

Controlling domain formation through defects

Experiments show that cooperative buckling among neighbouring
beams during lithiation leads to the formation of identical sinusoidal
buckling patterns within multiple domains; geometric incompatibili-
ties between separate domains induce mode-II buckling of beams at
the domain boundaries. We hypothesize that local defects drive the
particular buckling configuration of each domain. For example, two
types of defect in as-fabricated Si microlattices are node misalignments
during lattice stitching by two-photon lithography (Fig. 4c) and initial
beam curvature due to residual stresses within the Ni and Si layers
(Fig. 4d). To investigate the role of defects in cooperative buckling,
we constructed a 2D chemo-mechanical FEA model of an extended
unit cell with appropriate boundary conditions and introduced spe-
cific defects in the simulations. Each defect is represented as a small
pre-existing curvature with a mid-span displacement of 100 nm
(Supplementary Information section IX and Supplementary Video 9).

Figure 4a, b shows an overlay of FEA simulations and SEM images of
typical cooperatively buckled beams within a domain (Fig. 4a) and dis-
torted beams around a domain boundary (Fig. 4b). The red-coloured
beams on the left side of the extended unit cell, as illustrated in Fig. 4a
inset, are prescribed coherent defects that would favour node 1 rotating
anticlockwise and node 2 clockwise. The FEA simulation shows that
these nodes rotate as prescribed, and coherent buckling propagates
to the remaining defect-free beams in the extended unit cell through
coupling of beams at each node, which drives node 3 to rotate clockwise

and node 4 anticlockwise. In this case, all nearest-neighbour nodes
rotate in mutually opposite directions, and all beams form a coher-
ent sinusoidal pattern with pairwise opposite concavity (Fig. 4a). In
the second case (Fig. 4b), additional defects are prescribed to favour
nodes 3 and 4 rotating in the same directions as nodes 1 and 2 respec-
tively, as illustrated by the blue-coloured beams in Fig. 4b inset. The
FEA simulation predicts that the two defect-free beams in the cen-
tre of the extended unit cell will deform via mode-II buckling due to
geometric frustration, which has higher elastic energy, as quantified
by the reduced-order model (Supplementary Information section X).
These simulated responses to prescribed defects agree with experi-
mental observations, as evidenced by the underlying SEM images of
typical buckling patterns within and between domains (Fig. 4a, b),
with one notable distinction: vertical posts near domain boundaries
in experiments leaned slightly off-centre as a result of imbalanced forces
imposed by horizontal beams. These simulations reveal that fabrication
defects influence the nucleation of buckling domains locally during
lithiation. Short-range cooperative interactions among buckled beams
drive the propagation of ordered domains throughout the lattice. When
separate domains impinge on one another, they either coalesce to
form larger domains if compatible or generate domain boundaries if
mismatched, a process similar to the island growth model of metal
thin films[32].

Building upon the uncovered mechanism of defect-governed domain
formation in Si microlattices, we designed and incorporated a peri-
odic arrangement of artificial defects in Si microlattices (Extended
Data Fig. 3 and Supplementary Information section VI). Each arti-
ficial defect was a 5-μm-long, 100-nm-thick patch added on one side
of a polymer beam during two-photon lithography (Fig. 4e, f), which
caused the beam to buckle towards the other side during lithiation.
The single-domain pattern of Fig. 4g demonstrates that these periodic
artificial defects dominated over random fabrication defects during
lithiation-induced cooperative buckling. Furthermore, domain bound-
aries can be programmed to form arbitrary patterns by engineering
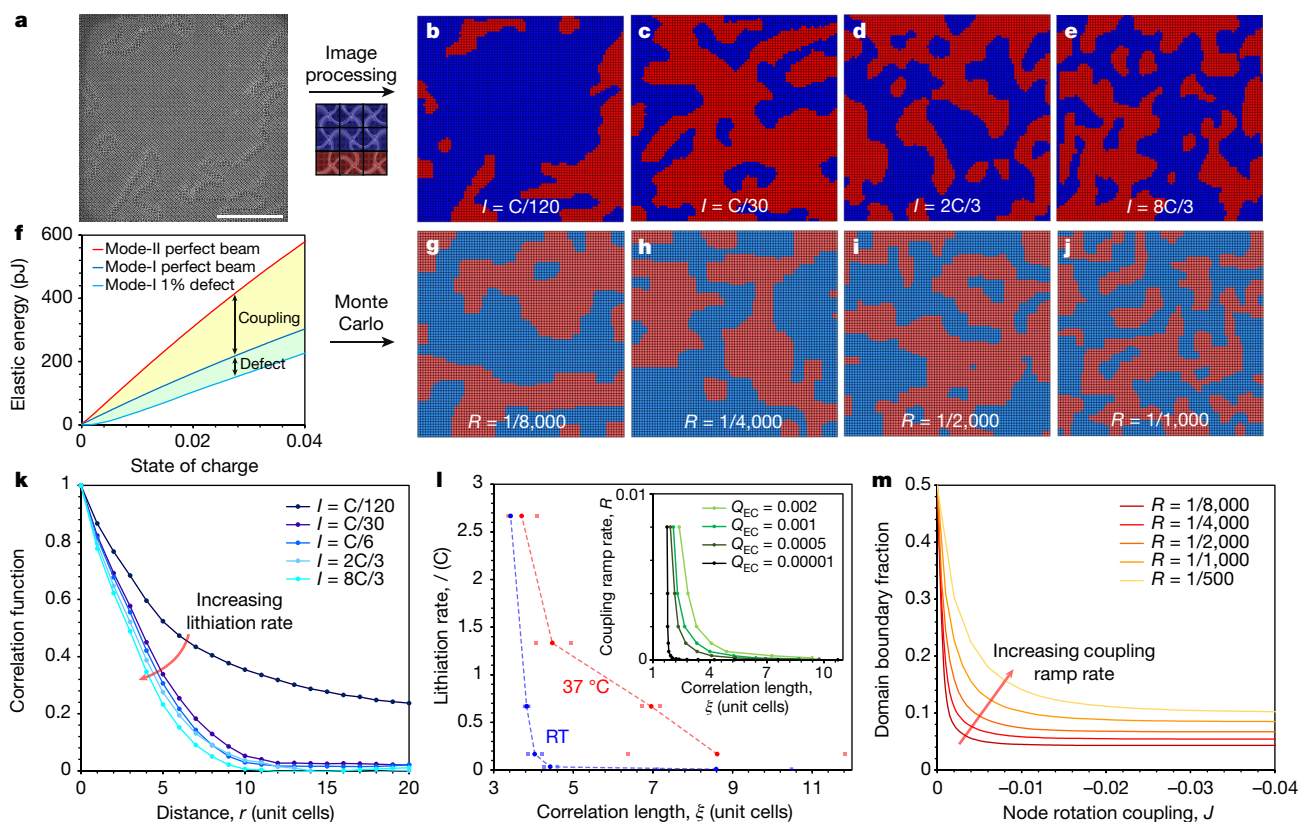
Fig. 5 | Statistical mechanics analysis of domain formation dynamics. **a**, SEM image of a Si microlattice lithiated at C/120, with an illustration of how the domain map in **b** is generated from **a**. Scale bar: 500 μm. **b–e**, Computer-processed domain maps of Si microlattices lithiated at progressively higher rates I from C/120 to 8C/3 at room temperature. Red and blue domains represent the two buckling phases that are mismatched by one unit cell. **f**, Elastic energy from the reduced-order model as a function of state of charge for three beam geometries: a perfect beam undergoing mode-II buckling (red), a perfect beam undergoing mode-I buckling (blue), and a beam with 1% imperfection undergoing mode-I buckling (light blue). The energy difference between mode-I and mode-II buckling for a perfect beam (yellow area) defines coupling of neighbouring nodes. The energy difference between a perfect beam and a beam with 1% imperfection undergoing mode-I buckling (green area) represents the energy contribution of the fabrication defect. **g–j**, Representative

domain maps generated by MC simulations for node coupling ramp rates R from 1/8,000 to 1/1,000 with electrochemical energy fluctuations $Q_{EC} = 0.001$. **k**, Statistical correlation function $C(r)$ of pairwise node rotations as a function of separation distance r for five different lithiation rates at room temperature. Data points are connected by straight lines. **l**, Variations in correlation length ξ with lithiation rate I for experiments conducted at room temperature (RT; blue) and at 37 °C (red). Circular data points connected by dotted lines are fitted from correlation functions that averaged two samples. Individually fitted correlation lengths for each sample are also shown as square data points. Inset, simulated variations in correlation length ξ with node coupling ramp rate R for four different electrochemical energy fluctuations Q_{EC}; data points are connected by straight lines. **m**, Fraction of domain boundaries, represented by the ratio of mode-II buckled beams, as a function of node rotation coupling J for five different coupling ramp rates R.

incompatible artificial defects to drive pairs of domains to join together at designated artificial-defect-free beams, which are forced to deform by mode-II buckling. To illustrate this concept, we constructed a digital bitmap of artificial defects to program a Caltech icon, which was indistinguishable in the as-fabricated lattice and emerged upon lithiation (Fig. 4h and Supplementary Video 5).

Statistical mechanics of domain distribution

To probe the domain formation dynamics, we lithiated Si microlattices at different rates. Figure 5a contains one example of SEM images that were computer-processed to construct pixelated domain maps of Si microlattices lithiated at progressively higher rates, as shown in Fig. 5b–e (see Extended Data Fig. 4 and Supplementary Information section VII for details). Each pixel in a domain map represents one of the 80 × 80 array of nodes in the sample: within a blue or red domain, all nearest-neighbour nodes rotate in phase in mutually opposite directions with all beams deformed by mode-I buckling; across the blue–red boundary, the interfacing nodes rotate in the same direction, which deforms the adjoining beam via mode-II buckling. Despite the arbitrary domain shapes, a clear trend of higher lithiation rates leading to smaller domains can be identified. To quantify average domain sizes, we computed the correlation[33,34] of node rotations as a function of their

separation distance $C(r) = \langle (-1)^r \cdot s_i \cdot s_{i+r} \rangle$, where $s_i = \pm 1$ for clockwise and anticlockwise node rotations, and $\langle \dots \rangle$ denotes an average of all node pairs separated by a distance r (Extended Data Fig. 5). Figure 5k compares correlation functions at five different lithiation rates at room temperature, each representing an average of two samples. It shows that a higher lithiation rate causes a faster decay in correlation between node rotations, which indicates a statistically smaller average domain size. Fitting an exponential function form, $C(r) = A\exp\left(-\dfrac{r}{\xi}\right)$, to these correlation functions allows us to determine the correlation length ξ, characteristic of the average domain size, for each lithiation rate at room temperature (blue curve in Fig. 5l) and at 37 °C (red curve in Fig. 5l). For both temperatures, correlation length decreases with higher lithiation rate; at an elevated temperature of 37 °C, a given lithiation rate leads to a larger correlation length than that at room temperature.

To gain insights about this lithiation-rate-dependent domain formation process, we studied the analogy between lithiation-induced cooperative buckling and the square-lattice antiferromagnetic Ising model[33–37]. This simplified statistical mechanics model qualitatively takes into consideration: (1) mechanical coupling between neighbouring nodes; (2) fabrication defects; (3) energy fluctuations intrinsic to chemical reactions; and (4) the rate of lithiation and deformation. We represent the energy of each microlattice as:
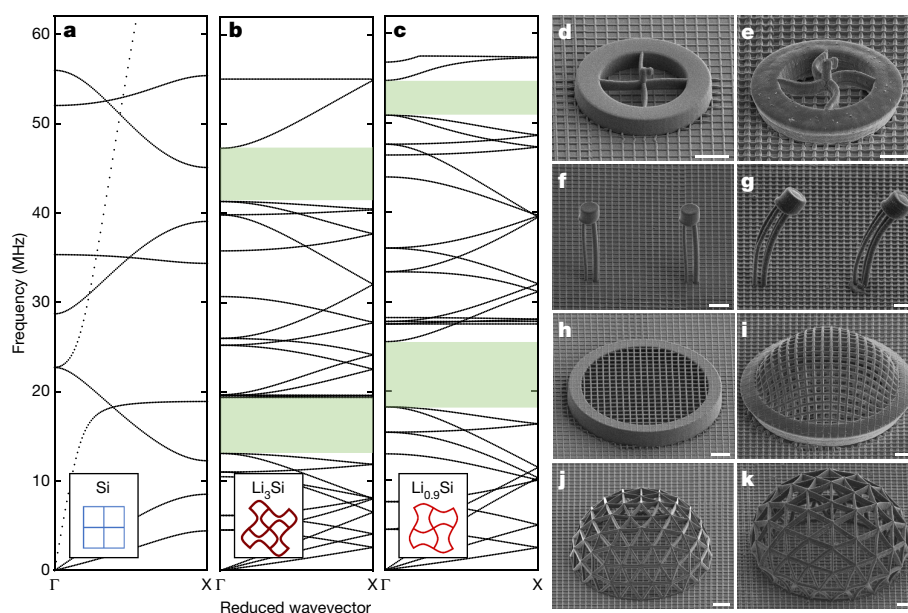
Fig. 6 | Outlook for electrochemically reconfigurable architected materials. a–c, Simulated phononic dispersion relations of as-fabricated Si microlattices (**a**), lithiated Li_3Si microlattices (**b**) and partially delithiated $Li_{0.9}Si$ microlattices (**c**) using Bloch boundary conditions. Points Γ to X in the Brillouin zone correspond to waves propagating in the x or y direction of the microlattices. Insets represent the chemical composition and the degree of buckling for each simulation. **d–k**, SEM images of electrochemically driven micro-architectures that reconfigure via rotation (**d**, **e**), bending (**f**, **g**), out-of-plane buckling (**h**, **i**) and structural expansion (**j**, **k**) in response to lithiation at a tilt angle of 52°. Left, as-fabricated; right, lithiated. Scale bars: 15 μm.

$$E(s) = -\sum_{\langle i,j \rangle} J \cdot s_i s_j - \sum_i h_i \cdot s_i \qquad (1)$$

where J represents the coupling between nearest-neighbour node rotations, and h_i represents the influence of a random fabrication defect at each node. Figure 5f shows that the lower elastic energy of mode-I buckling compared with mode-II buckling gives rise to the coupling between two nearest-neighbour nodes that favours opposite rotations. Figure 5f also shows that the strength of such coupling increases gradually from zero to a finite value as lithiation progresses (yellow area), and so does the energy contribution of a fabrication defect (green area). In addition to the mechanical interactions described in equation (1), we postulate that there exists an effective level of energy fluctuations Q_{EC} in the local electrochemical environment around each node. Q_{EC} can be understood as the result of a stochastic perturbation of the competing force balance on the two opposite surfaces of a bistable beam due to local lithiation nucleation events before it buckles irreversibly in a particular direction (Supplementary Information section VIII).

Monte Carlo (MC) simulations of the statistical mechanics model were implemented with random initial node rotations (Supplementary Information section VIII). We gradually turned on node rotation coupling J from zero to a normalized value of -1 and the influence of fabrication defects h_i across all nodes from zero to a normal distribution with a mean of 0 (that is, equal probability for either direction) and a standard deviation of 0.125. Both J and h_i were ramped up by a total of N_{incr} increments with a linear ramp rate defined as $R = 1/N_{incr}$. At each increment, we evolved the system by 6,400 MC steps using the Metropolis algorithm. In each MC step, a random node is chosen and flipped: if the resulting system energy change $\Delta E < 0$, the trial is accepted; if $\Delta E > 0$, the trial is accepted with a probability $P = \exp\left(-\frac{\Delta E}{Q_{EC}}\right)$. Figure 5g–j shows representative domain maps generated by simulations with $Q_{EC} = 0.001$ at progressively higher coupling ramp rates R that result in progressively smaller domains. Figure 5m shows that as the coupling J is turned on in each lattice, the fraction of domain boundaries drops rapidly due to the growth of domains, and stabilize when J is relatively large compared with Q_{EC} but roughly two orders of magnitude smaller than its final value of -1.

Figure 5m also shows that at a slower coupling ramp rate R, the domain boundary fraction stabilizes at a lower value indicative of larger domains. The relationship between coupling ramp rate R and correlation length ξ is shown in Fig. 5l inset for four different Q_{EC} values from 0.00001 to 0.002, where each ξ is derived by fitting of the averaged correlation function from ten simulations. It reveals that higher coupling ramp rates lead to smaller correlation lengths for each Q_{EC}, and that a higher Q_{EC} shifts this relation towards larger correlation lengths. Extensive simulations with different $Q_{EC} \ll 1$ and $h_i < 1$ convey the same qualitative trends (Extended Data Fig. 6a–c).

The proposed statistical mechanics model shows reasonable agreement with experimental results (Fig. 5l) and provides valuable insights about domain formation dynamics. MC simulations reveal that minute energy fluctuations play an important role in domain growth when node rotation coupling is turned on gradually. In Si microlattices undergoing lithiation, the amplitude of energy fluctuations caused by electrochemistry is orders of magnitude smaller than stored elastic energy in the beams. In this regime of $Q_{EC} \ll J_{final}$, the final coupling strength becomes irrelevant to domain formation because domain boundaries stabilize at J such that $Q_{EC} < J \ll J_{final}$ (Fig. 5m), and only the ratio of coupling ramp rate R and Q_{EC} governs formed domain sizes (Extended Data Fig. 6d). At lower coupling ramp rates, the system effectively stays longer in an environment where energy fluctuations remain relevant and relaxes into a lower energy state with larger domains. Increasing the electrochemical energy fluctuations also allows the domains to grow larger by extending the range of coupling strength subject to these energy fluctuations. This rate-dependent interplay between mechanical node rotation coupling and electrochemical energy fluctuations during the initial stage of lithiation-induced cooperative buckling is prohibitively challenging to observe experimentally. The discussion here provides a new perspective within which to utilize statistical mechanics tools to qualitatively explain and predict the dynamic response of architected materials with defect- and fluctuation-sensitive instabilities. It highlights the intriguing similarities between architected materials and classical materials so that we could potentially draw inspiration from established theories, such as phase transformations and metallurgy (for example, annealing and quenching to control grain size), to guide the design of architected materials.

Discussion and outlook

The demonstrated electrochemically driven cooperative buckling in Si microlattices uncovers a new regime for dynamic structural reconfiguration in architected materials. Most of the existing reconfigurable architected materials are soft polymer structures that rely on persistent external stimuli to stay in the deformed geometry[2,8,9,13,14,17,38] or are multi-stable in discrete configurations[11,12,39,40] (Extended Data Table 1 and Supplementary Information section XII). The Si microlattices in this work are electrochemically lithiated to induce simultaneous elastic buckling and plastic deformation, which enables non-volatile reconfiguration in stiff architected materials. The degree of buckling can be continuously modulated and reversed by simple electrical control. We demonstrated that systematically incorporated buckling instabilities can accommodate large volumetric expansions that often imperil the mechanical stability of beyond-intercalation battery electrodes. This stress relief mechanism via buckling is largely independent of the intrinsic post-elastic deformability of electrode materials and is not subject to plastic energy dissipation and strain rate sensitivity, which opens possibilities of using this approach with brittle electrode materials like sulphur. Optimizing architecture design could increase the energy density and potentially enable multi-functional capabilities for on-chip or implantable energy storage systems.

Through the interactions among neighbouring beams, cooperative buckling transforms a simple tetragonal lattice into a sinusoidal lattice with intriguing mechanical metamaterial properties, which is discussed here as an example of the capabilities of electrochemically reconfigurable architected materials. These buckled structures have been shown to have a negative Poisson's ratio upon lateral deformation[38,41,42], and deform synclastically upon out-of-plane bending[43]. For elastic vibrations, they provide an efficient platform for designing tunable phononic crystals. To illustrate this point, we constructed a finite element model to examine changes in phononic dispersion relations for in-plane elastic wave propagation in Si microlattices upon lithiation (Supplementary Information section XI). Figure 6a–c and Extended Data Fig. 7 demonstrate that lithiation-induced cooperative buckling creates two 6-MHz-wide bandgaps centred at 16 MHz and 44 MHz for waves propagating in all in-plane directions. Upon partial delithiation, the centre frequencies of the bandgaps shift by 6 MHz and 9 MHz, respectively. The formation and the set-and-hold tunability of these bandgaps are attributed to both the structural transformations and the changes in material properties caused by electrochemical reactions. We consider that such tunable phononic bandgaps of architected materials, combined with the versatility of additive manufacturing, could empower novel microelectromechanical systems (MEMS)[44]. Defect engineering, as demonstrated in this work, allows for accurate programming of distorted domain boundaries between ordered domains in which elastic wave propagation at certain frequencies is forbidden. This opens up opportunities to trap and control phonon modes inside the domain boundaries, which could potentially enable topological metamaterials[45,46].

Complex, tailor-made reconfigurability can be designed for non-periodic architectures by controlling the relative ratio of the polymer scaffold and the active material as well as mechanical constraints. Figure 6d–k illustrates exemplar building blocks with rotational, bending, out-of-plane buckling, and expansive degrees of freedom induced by electrochemical lithiation. Even though the material systems used in this work are air-sensitive, other alloying systems and redox couples with compatible phase diagrams and realistic diffusion kinetics can be explored in aqueous electrolytes[47] or even bodily fluids[48,49]. For electrochemical discharge reactions like Si-Li alloying, the structural reconfiguration process releases energy in the form of electrical current, which can be used for simultaneous heating or communication. Bio-implantable applications and self-deployable micro-devices are of particular interest because of the requirements of large geometric transformations and the constant bodily environments that are insensitive to (or unreachable by) external stimuli.

In summary, we have designed and fabricated reconfigurable architected materials based on electrochemically driven cooperative beam buckling. The large volumetric expansion and contraction of electrochemical alloying and dealloying reactions served as the driving force for stable, continuous and reversible structural transformations through coupled mechanical instabilities. Chemo-mechanical models revealed the dynamic interplay among different deformation mechanisms and provided design guidelines to control the instability of individual beams. We discovered and demonstrated that defects play a governing role in nucleation and growth of transformed domains during cooperative buckling, analogous to polycrystalline metal thin film growth. We used statistical mechanics tools to analyse the stochastic domain formation process and implanted artificial defects to precisely program the shape of domain boundaries. This framework of designing, fabricating, modelling, predicting and programming dynamic architected materials could inspire new pathways towards smart, multifunctional materials in the future.

Online content

1. Krödel, S., Delpero, T., Bergamini, A., Ermanni, P. & Kochmann, D. M. 3D auxetic microlattices with independently controllable acoustic band gaps and quasi-static elastic moduli. *Adv. Eng. Mater.* **16**, 357–363 (2014).
2. Babaee, S. et al. 3D soft metamaterials with negative Poisson's ratio. *Adv. Mater.* **25**, 5044–5049 (2013).
3. Valentine, J. et al. Three-dimensional optical metamaterial with a negative refractive index. *Nature* **455**, 376–379 (2008).
4. He, H. et al. Topological negative refraction of surface acoustic waves in a Weyl phononic crystal. *Nature* **560**, 61–64 (2018).
5. Meza, L. R., Das, S. & Greer, J. R. Strong, lightweight, and recoverable three-dimensional ceramic nanolattices. *Science* **345**, 1322–1326 (2014).
6. Bauer, J., Schroer, A., Schwaiger, R. & Kraft, O. Approaching theoretical strength in glassy carbon nanolattices. *Nat. Mater.* **15**, 438–443 (2016).
7. Dou, N. G., Jagt, R. A., Portela, C. M., Greer, J. R. & Minnich, A. J. Ultralow thermal conductivity and mechanical resilience of architected nanolattices. *Nano Lett.* **18**, 4755–4761 (2018).
8. Overvelde, J. T. B., Weaver, J. C., Hoberman, C. & Bertoldi, K. Rational design of reconfigurable prismatic architected materials. *Nature* **541**, 347–352 (2017).
9. Coulais, C., Teomy, E., De Reus, K., Shokef, Y. & Van Hecke, M. Combinatorial design of textured mechanical metamaterials. *Nature* **535**, 529–532 (2016).
10. Fu, H. et al. Morphable 3D mesostructures and microelectronic devices by multistable buckling mechanics. *Nat. Mater.* **17**, 268–276 (2018).
11. Shan, S. et al. Multistable architected materials for trapping elastic strain energy. *Adv. Mater.* **27**, 4296–4301 (2015).
12. Haghpanah, B., Salari-Sharif, L., Pourrajab, P., Hopkins, J. & Valdevit, L. Multistable shape-reconfigurable architected materials. *Adv. Mater.* **28**, 7915–7920 (2016).
13. Kang, S. H. et al. Buckling-induced reversible symmetry breaking and amplification of chirality using supported cellular structures. *Adv. Mater.* **25**, 3380–3385 (2013).
14. Sydney Gladman, A., Matsumoto, E. A., Nuzzo, R. G., Mahadevan, L. & Lewis, J. A. Biomimetic 4D printing. *Nat. Mater.* **15**, 413–418 (2016).
15. Kang, S. H. et al. Complex ordered patterns in mechanical instability induced geometrically frustrated triangular cellular structures. *Phys. Rev. Lett.* **112**, 098701 (2014).
16. Liu, J. et al. Harnessing buckling to design architected materials that exhibit effective negative swelling. *Adv. Mater.* **28**, 6619–6624 (2016).
17. Kim, Y., Yuk, H., Zhao, R., Chester, S. A. & Zhao, X. Printing ferromagnetic domains for untethered fast-transforming soft materials. *Nature* **558**, 274–279 (2018).
18. Coulais, C., Kettenis, C. & van Hecke, M. A characteristic length scale causes anomalous size effects and boundary programmability in mechanical metamaterials. *Nat. Phys.* **14**, 40–44 (2018).
19. Bertoldi, K., Vitelli, V., Christensen, J. & van Hecke, M. Flexible mechanical metamaterials. *Nat. Rev. Mater.* **2**, 17066 (2017).
20. Kelly, A. & Knowles, K. M. *Crystallography and Crystal Defects* (Wiley & Sons, 2012).
21. McDowell, M. T., Lee, S. W., Nix, W. D. & Cui, Y. 25th anniversary article: Understanding the lithiation of silicon and other alloying anodes for lithium-ion batteries. *Adv. Mater.* **25**, 4966–4985 (2013).
22. Liu, X. H. et al. Self-limiting lithiation in silicon nanowires. *ACS Nano* **7**, 1495–1503 (2013).

23. Baggetto, L., Danilov, D. & Notten, P. H. L. Honeycomb-structured silicon: remarkable morphological changes induced by electrochemical (de)lithiation. *Adv. Mater.* **23**, 1563–1566 (2011).
24. Bhandakkar, T. K. & Johnson, H. T. Diffusion induced stresses in buckling battery electrodes. *J. Mech. Phys. Solids* **60**, 1103–1121 (2012).
25. Obrovac, M. N. & Chevrier, V. L. Alloy negative electrodes for Li-ion batteries. *Chem. Rev.* **114**, 11444–11502 (2014).
26. Huang, S. & Zhu, T. Atomistic mechanisms of lithium insertion in amorphous silicon. *J. Power Sources* **196**, 3664–3668 (2011).
27. Chan, C. K. et al. High-performance lithium battery anodes using silicon nanowires. *Nat. Nanotechnol.* **3**, 31–35 (2008).
28. Liu, J. et al. Mechanically and chemically robust sandwich-structured C@Si@C nanotube array Li-ion battery anodes. *ACS Nano* **9**, 1985–1994 (2015).
29. Di Leo, C. V., Rejovitzky, E. & Anand, L. Diffusion–deformation theory for amorphous silicon anodes: the role of plastic deformation on electrochemical performance. *Int. J. Solids Struct.* **67–68**, 283–296 (2015).
30. Wu, H. et al. Stable cycling of double-walled silicon nanotube battery anodes through solid-electrolyte interphase control. *Nat. Nanotechnol.* **7**, 310–315 (2012).
31. Xia, X., Di Leo, C. V., Gu, X. W. & Greer, J. R. In situ lithiation-delithiation of mechanically robust Cu-Si core-shell nanolattices in a scanning electron microscope. *ACS Energy Lett.* **1**, 492–499 (2016).
32. Nix, W. D. & Clemens, B. M. Crystallite coalescence: a mechanism for intrinsic tensile stresses in thin films. *J. Mater. Res.* **14**, 3467–3473 (1999).
33. Nowak, U. & Usadel, K. D. Structure of domains in random Ising magnets. *Phys. Rev. B* **46**, 8329–8335 (1992).
34. Landau, D. P. & Binder, K. *A Guide to Monte Carlo Simulations in Statistical Physics* (Cambridge Univ. Press, 2015).
35. Sahni, P. S., Grest, G. S., Anderson, M. P. & Safran, S. A. Kinetics of ordering in two dimensions. II. Quenched systems. *Phys. Rev. B* **28**, 2705–2716 (1983).
36. Cornell, S. & Stinchcombe, R. Freezing in a two-dimensional Glauber system under continuous cooling. *Phys. Rev. B* **45**, 2725–2738 (1992).
37. Shokef, Y., Souslov, A. & Lubensky, T. C. Order by disorder in the antiferromagnetic Ising model on an elastic triangular lattice. *Proc. Natl Acad. Sci. USA* **108**, 11804–11809 (2011).
38. Chen, Y., Li, T., Scarpa, F. & Wang, L. Lattice metamaterials with mechanically tunable Poisson's ratio for vibration control. *Phys. Rev. Appl.* **7**, 024012 (2017).
39. Restrepo, D., Mankame, N. D. & Zavattieri, P. D. Phase transforming cellular materials. *Extreme Mech. Lett.* **4**, 52–60 (2015).
40. Correa, D. M. et al. Negative stiffness honeycombs for recoverable shock isolation. *Rapid Prototyp. J.* **21**, 193–200 (2015).
41. Körner, C. & Liebold-Ribeiro, Y. A systematic approach to identify cellular auxetic materials. *Smart Mater. Struct.* **24**, 025013 (2015).
42. Clausen, A., Wang, F., Jensen, J. S., Sigmund, O. & Lewis, J. A. Topology optimized architectures with programmable Poisson's ratio over large deformations. *Adv. Mater.* **27**, 5523–5527 (2015).
43. Liebold-Ribeiro, Y. & Körner, C. Phononic band gaps in periodic cellular materials. *Adv. Eng. Mater.* **16**, 328–334 (2014).
44. Cha, J. & Daraio, C. Electrical tuning of elastic wave propagation in nanomechanical lattices at MHz frequencies. *Nat. Nanotechnol.* **13**, 1016–1020 (2018).
45. Süsstrunk, R. & Huber, S. D. Observation of phononic helical edge states in a mechanical topological insulator. *Science* **349**, 47–50 (2015).
46. Süsstrunk, R. & Huber, S. D. Classification of topological phonons in linear mechanical metamaterials. *Proc. Natl Acad. Sci. USA* **113**, E4767–E4775 (2016).
47. Fahrenkrug, E., Gu, J. & Maldonado, S. Electrochemically gated alloy formation of crystalline InAs thin films at room temperature in aqueous electrolytes. *Chem. Mater.* **26**, 4535–4543 (2014).
48. Wang, Y., Xu, H., Zhang, J. & Li, G. Electrochemical sensors for clinic analysis. *Sensors* **8**, 2043–2081 (2008).
49. Jager, E. W. H., Smela, E. & Ingana, O. Microfabricating conjugated polymer actuators. *Science* **290**, 1540–1545 (2000).

METHODS

Two-photon lithography of polymer microlattices. Tetragonal lattices with unit cells of size 20 μm × 20 μm × 5 μm (along x-, y- and z-axes, respectively) are designed in MATLAB and imported into a commercial two-photon lithography system (Photonic Professional GT, Nanoscribe). Each sample consists of a 10 × 10 array of stitched smaller lattices written sequentially because of the limited writing area of the two-photon lithography system. Each smaller tetragonal lattice has 8 × 8 × 5 unit cells, and stitched lattices overlap by one unit cell. Therefore, each sample has 79 × 79 × 5 unit cells in total, written on a cleaned glass coverslip substrate (18 mm diameter circular No. 2 glass, VWR) with a custom-made photoresist. This negative photoresist is composed of 79.1 wt% Acrylo POSS monomer (MA0736, Hybrid Plastics), 20.0 wt% dichloromethane solvent (Sigma-Aldrich), and 0.9 wt% 7-diethylamino-3-thenoylcoumarin photoinitiator (Luxottica Exciton), and it is placed on top of the glass substrate. Immersion oil is used between the 63× objective of the two-photon lithography system and the bottom side of the glass substrate. After two-photon lithography, the sample is developed in PGMEA (propylene glycol monomethyl ether acetate, Sigma-Aldrich) for 25 min, and then rinsed three times in isopropanol before critical point drying. Each polymer sample has horizontal beams of elliptical cross-section with a vertically aligned major axis of ~1.8 μm and a minor axis of ~0.5 μm, and cylindrical vertical posts with a diameter of ~1.8 μm with small sample-to-sample variations due to two-photon lithography laser degradation. The bottom layer of the vertical posts is extended to 10 μm to assist the twisting of the vertical posts during lithiation, and in the bottom 3 μm of these vertical posts, the diameter gradually increases to ~3.6 μm to enhance adhesion with the substrate.

Si microlattice fabrication. The polymer samples are cleaned by oxygen plasma and baked for 2 h at 250 °C in an Ar-filled glovebox before RF magnetron sputtering deposition on the lattice beams of ~5 nm of a Cr seed layer and ~100 nm of a Ni conductive layer (100 W, 20 sccm Ar flow, 5 mtorr deposition pressure, AJA International). The sputtered Ni film is thicker at the top of each horizontal beam and thinner at the bottom. Next, ~300 nm of amorphous Si is deposited by plasma enhanced chemical vapour deposition (PECVD, Oxford Instruments) under the following conditions: 200 °C temperature, 400 mtorr pressure, 250 sccm of 5% silane in Ar precursor gas flow, and 10 W RF power. A shadow mask with a 1.8 mm square opening is used during PECVD to limit Si deposition to the lattice section only. Finally, ~100 nm of Ni thin film is coated on the back of the sample substrate by sputtering, ensuring a good electrical pathway to the Ni layer on top of the substrate through sufficient Ni coverage on the edge of the substrate. The total Si mass loading on a representative sample is measured by Cahn C-35 microbalance to be 8.0 ± 0.4 μg by mass measurements before and after KOH etching of Si on the lattice. Part of the substrate has to be cut off by a diamond pen to keep the total sample mass within the range with 0.1 μg sensitivity, so measuring Si mass for each sample before electrochemical testing is not practical. We note variation of Si mass loading occurs across samples due to two-photon lithography laser degradation and PECVD chamber conditions during Si deposition. The areal Si mass loading calculated from the area of the Si deposition shadow mask opening is ~0.25 mg cm^{-2}. The theoretical capacity for each Si microlattice sample is ~29 μAh based on the theoretical specific capacity[25] of silicon, which is 3,600 mAh per g Si. C-rates are approximated using a theoretical electrode capacity of 30 μAh.

Sn microlattice fabrication. To demonstrate that the electrochemically driven cooperative buckling is not specific to the Si-Li alloying chemistry, we fabricated Sn microlattices and observed a similar lithiation-induced cooperative buckling behaviour. Approximately 200 nm of Sn is deposited onto the polymer lattice by RF magnetron sputtering (75 W, 20 sccm Ar flow, 5 mtorr deposition pressure, AJA International). Owing to the low melting temperature of Sn, the sputtered Sn film is highly faceted and concentrated on the top of the horizontal beams with extruding crystalline grains of size ~1 μm. In this case, Sn functions as both active material and current collector. Despite large differences in surface morphologies between Sn and Si microlattice beams, the Sn microlattices also buckled cooperatively into the sinusoidal pattern upon lithiation-induced volumetric expansion.

Electrochemical testing. Modified CR2032 coin cells are used for cyclic voltammetry and long-term cycling with accurate electrochemical data and minimized side reactions (Extended Data Fig. 2a). A 0.79-mm-thick polyethylene washer is attached to the sample substrate via re-solidified paraffin wax (Sigma-Aldrich) to create a small leak-free cavity around the Si microlattice, which substantially reduces the amount of electrolyte and the contact area between electrolyte and Ni thin film on the substrate. Approximately 30 μl of electrolyte is used in each coin cell, and the electrolyte consists of 90 vol.% of 1 M LiPF$_6$ in ethylene carbonate/diethyl carbonate = 50/50 (v/v) (battery grade, Sigma-Aldrich) and 10 vol.% fluoroethylene carbonate additive (BASF). A Li counter electrode with a 25-μm-thick separator (Samsung) is placed on top of the polyethylene washer cavity filled with electrolyte. The modified coin cells are sealed by a crimper inside an Ar-filled glovebox before they are taken out for electrochemical testing.

A custom-made electrochemical cell with a quartz window is used for in situ optical observation (Extended Data Fig. 2b, c). A circular hole is punched in the Li foil to unblock the view from the top of the Si microlattice during in situ experiments. During electrochemical lithiation/delithiation, a Keyence VW-9000 digital microscope records the dynamics of cooperative buckling/unbuckling in the Si microlattices. Approximately 400 μl of 1 M LiPF$_6$ in ethylene carbonate/diethyl carbonate = 50/50 (v/v) (battery grade, Sigma-Aldrich) electrolyte is used for the in situ cell. This electrolyte amount gives rise to large side reactions from electrolyte decomposition and impurities such as water and oxygen, which leads to larger and inaccurate lithiation capacity in the in situ cell. Therefore, accurate electrochemical analysis and long-term cycling are conducted in modified coin cells.

Artificial defects. Figure 4e, f shows artificial defects prescribed in the 3D lattice design. These artificial defects are 5-μm-long and 100-nm-thick patches added to one side of the horizontal beams of the polymer lattice in a periodic fashion during two-photon lithography. This is achieved by writing a separate 5-μm-long beam in the middle of the horizontal beam 100 nm off the centre axis so the majority of the two beams overlap, producing the 100-nm-thick patch on one side. The subsequently deposited Ni and Si layers follow the surface morphology of the polymer beams. Such artificial defects are demonstrated to cause the beams to buckle towards the side without the additional patch. Within each unit cell, one pair of opposite beams have artificial defects facing towards each other, causing the beams to buckle away from each other; the other pair of opposite beams have artificial defects facing away from each other, causing the beams to buckle towards each other. Such periodic artificial defects on all layers of the horizontal beams or just the topmost layer overwhelm existing fabrication defects and control buckling directions deterministically. With the help of artificial defects, we can make lithiated Si microlattices in a single domain without any domain boundaries (Fig. 4g) or program any pattern to be formed by the domain boundaries (Fig. 4h). For the latter case, different sides of the designated domain boundaries are implanted with incompatible artificial defects of the two bistable domain phases and the beams at the domain boundaries are artificial-defect-free so they are forced to deform via mode-II buckling due to geometric frustration.

Domain map processing. SEM images of domain maps formed at different lithiation rates are processed digitally to analyse the correlation between node rotations. Domain boundaries on SEM images are first traced manually and then processed by MATLAB into an 80 × 80 array of nodes showing the distribution of the two bistable domain phases, as shown in red and blue in Fig. 5b–e. From this array, we can calculate the correlation of pairwise node rotations as a function of their separation in terms of the nearest integer number of unit cells. The decay of this correlation function with respect to the separation distance is characteristic of the average domain size in each domain map, where a faster decay indicates a smaller average domain size. Figure 5k shows the averaged correlation functions from two samples at each lithiation rate with a clear trend of a higher lithiation rate leading to a faster decay in correlation and therefore a smaller average domain size. We fitted an exponential decay function $C(r) = A\exp\left(-\frac{r}{\xi}\right)$ to the correlation functions in MATLAB to calculate the statistical correlation length ξ for each lithiation rate. The first ten points in each correlation function plot (distance $r \leq 9$) are used for the fitting due to the large statistical noise at larger distances where correlation is low.

Data availability
The data that support the findings of this study are available from the corresponding author upon reasonable request.

Author contributions X.X., C.V.D.L. and J.R.G. designed the study and interpreted the results. X.X. and J.R.G. conceived the idea of electrochemically driven cooperative buckling in architected materials. X.X. developed the fabrication process, fabricated all samples, and designed the experimental set-ups. X.X. and H.Y. conducted electrochemical testing and analysed the electrochemical data. A.A. and C.V.D.L. designed and conducted the coupled chemo-mechanical finite element simulations and the reduced-order simulations. X.X. analysed the domain maps and conducted the Monte Carlo simulations. C.M.P. and D.M.K.

Extended Data Fig. 1 | Sn microlattices before and after lithiation-induced cooperative beam buckling. a, **b**, SEM images of representative as-fabricated Sn microlattices. **c**–**f**, SEM images of representative Sn microlattices after lithiation, exhibiting a similar cooperative beam buckling behaviour. Images in **b**, **d** and **f** are taken at a tilt angle of 52°.

a

SS spring and spacer
Lithium
Separator and electrolyte
Polyethylene washer
Paraffin wax
Substrate coated with Ni
Coin cell casing

b

c
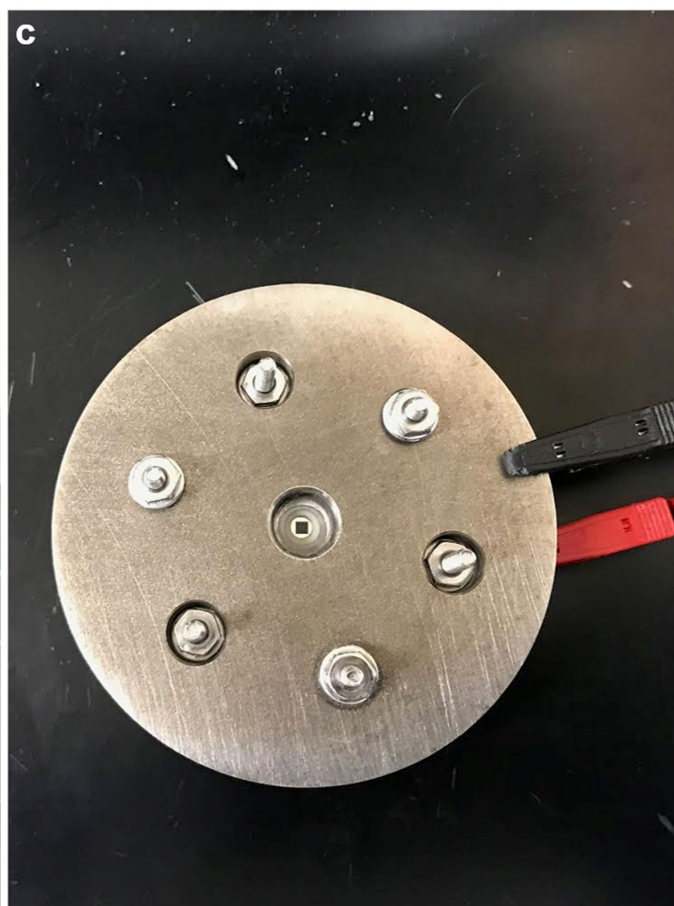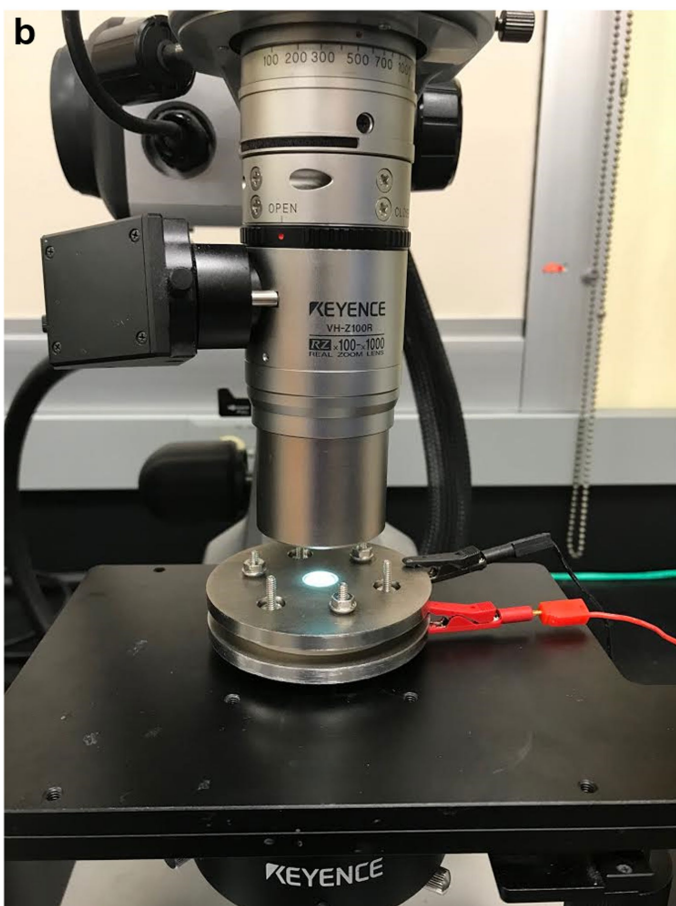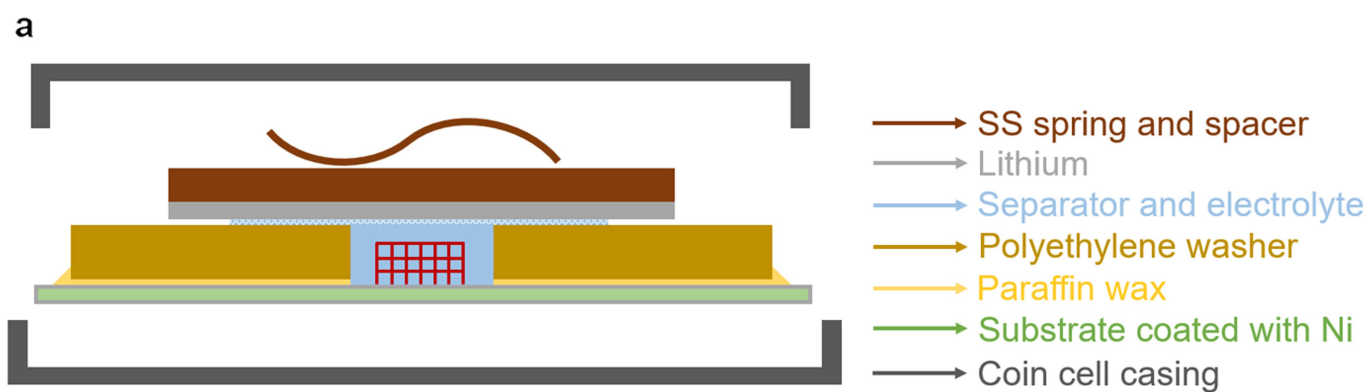
Extended Data Fig. 2 | Custom electrochemical testing set-up.
a, Illustration of modified CR2032 coin cells consisting of a stainless steel (SS) casing, a SS spring, a SS spacer, a separator, electrolyte, a polyethylene washer, paraffin wax, a Si microlattice sample on a glass substrate coated with Ni, and a Li counter electrode. **b**, **c**, Images of the in situ optical microscopy set-up and the custom electrochemical cell with a quartz viewing window. See Methods section 'Electrochemical testing' for details.
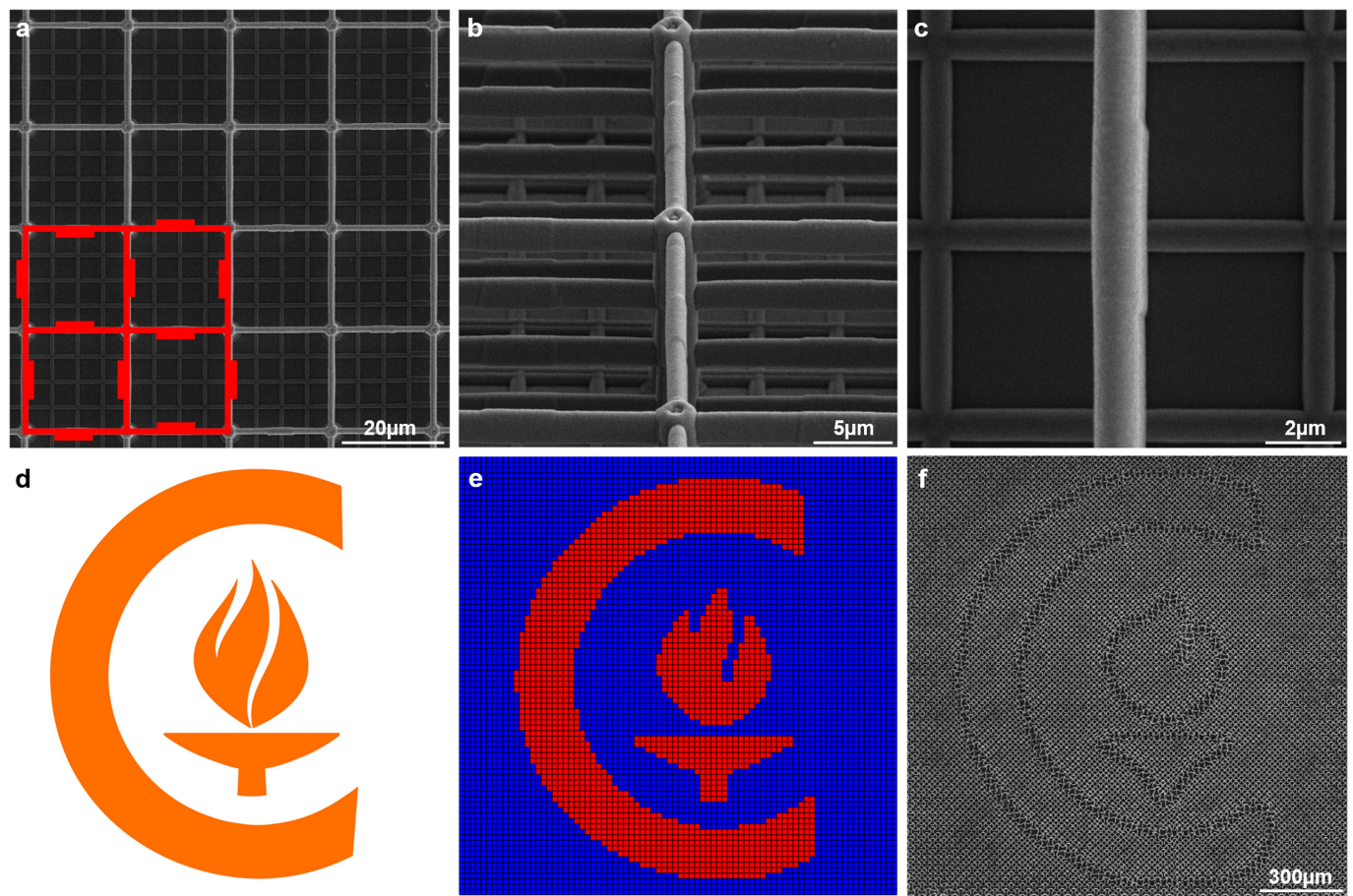
Extended Data Fig. 3 | Processing and implanting artificial defects based on the Caltech icon. a–c, SEM images of periodically arranged artificial defects. Each artificial defect is a 5-μm-long, 100-nm-thick patch on one side of a horizontal beam, as illustrated in red in **a**. **d**, Image of the Caltech icon. **e**, Processed domain map based on the Caltech icon. **f**, SEM image of programmed domain boundaries of the Caltech icon shape after lithiation, produced by pre-designing artificial defects. The Caltech icon is used with permission.
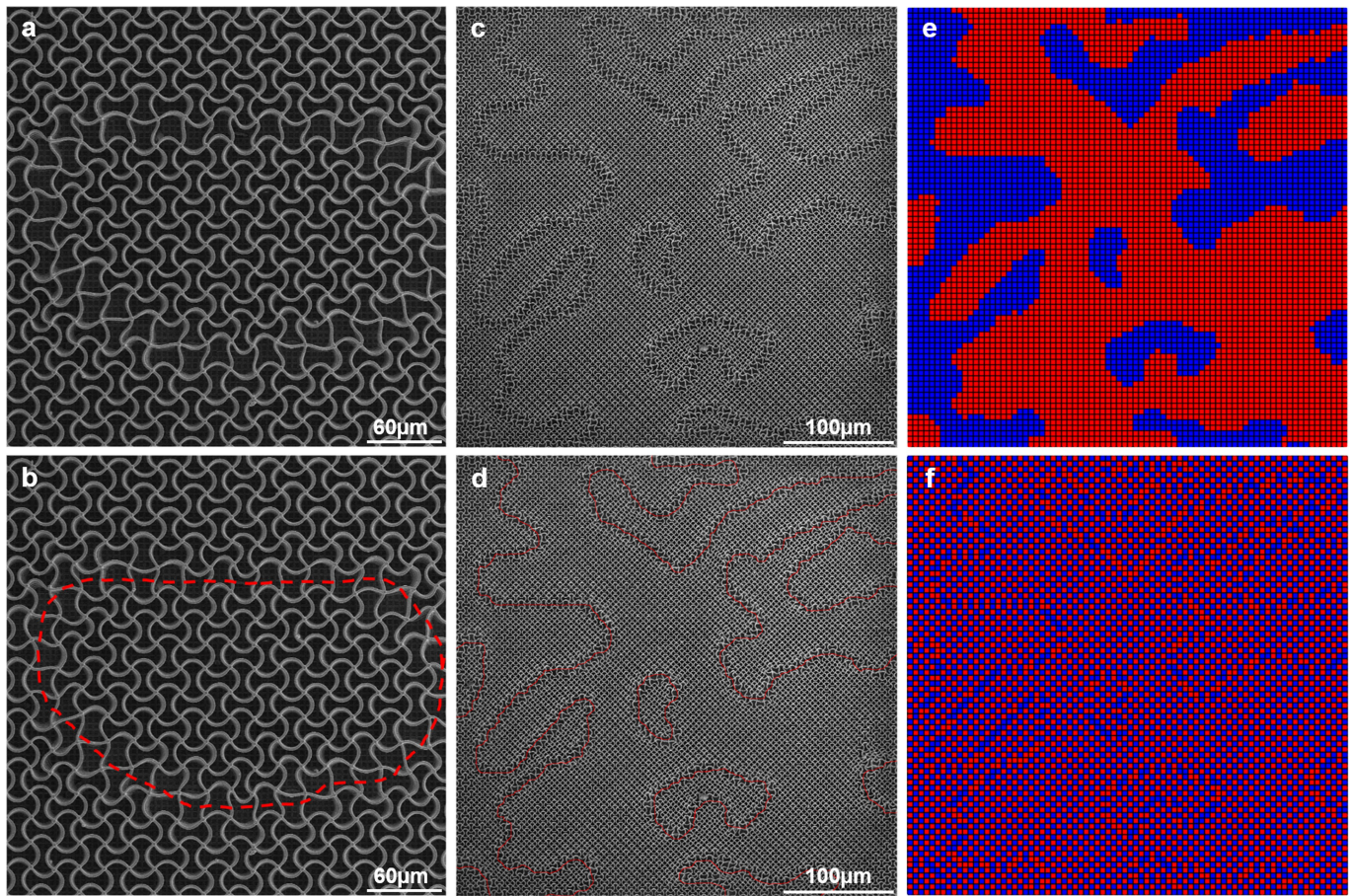
Extended Data Fig. 4 | Tracing of domain boundaries to generate digital domain maps. a, SEM image of a representative domain. **b**, Tracing the domain boundary (red dashed line) in **a** through mode-II buckled beams. **c**, SEM image of a representative lithiated Si microlattice sample with multiple domains. **d**, Tracing of domain boundaries on the original SEM image in **c**. **e**, An example of digitally processed domain maps with red and blue square pixels indicating each node being in one of the two bistable domain phases. **f**, An example of digitally processed node rotation maps with red and blue square pixels indicating respectively clockwise and anticlockwise rotation of each node, which can be represented mathematically by an 80×80 array of $s_i = \pm 1$ for clockwise and anticlockwise node rotations. From this array, we can calculate the correlation of pairwise node rotation directions as a function of their separation in terms of the nearest integer number of unit cells.
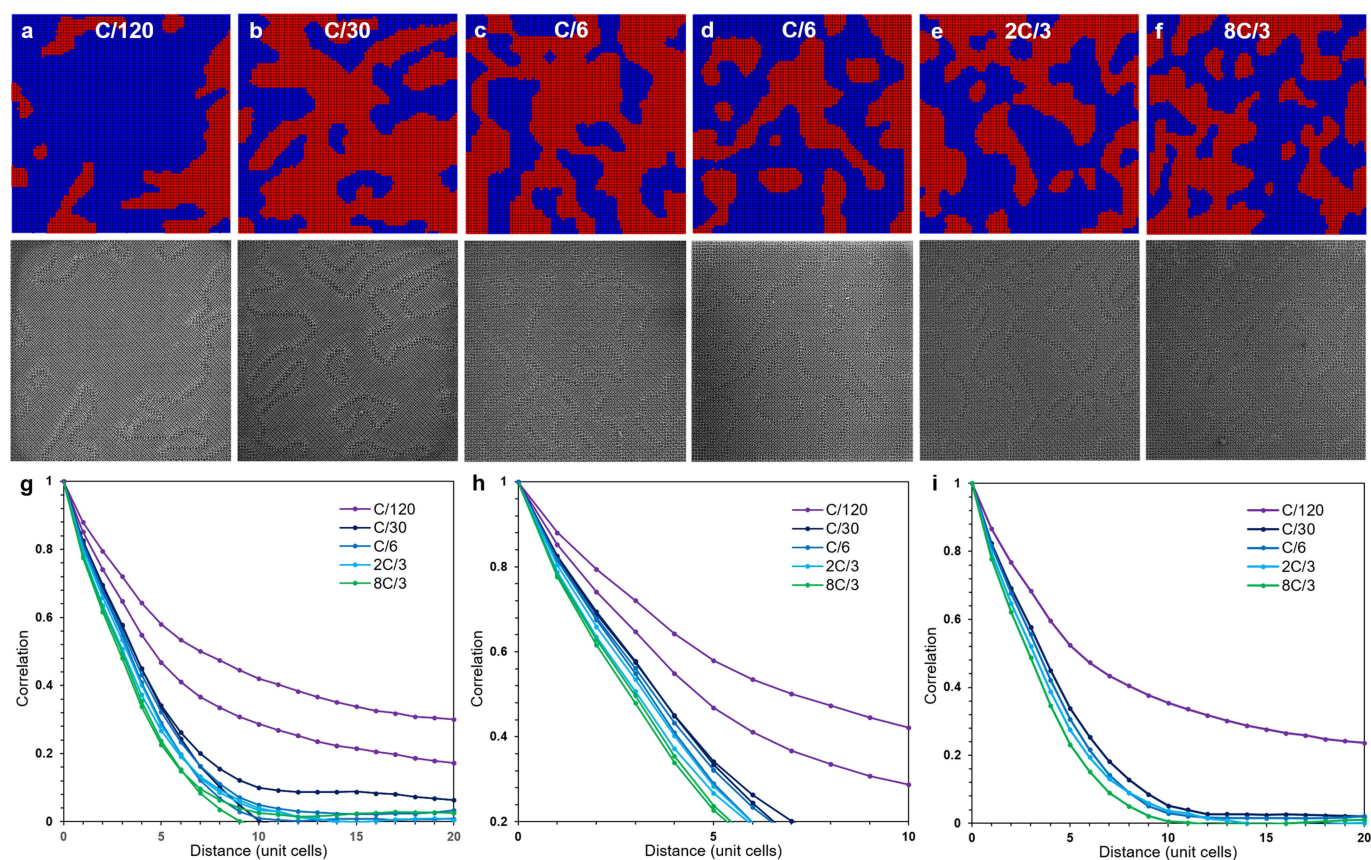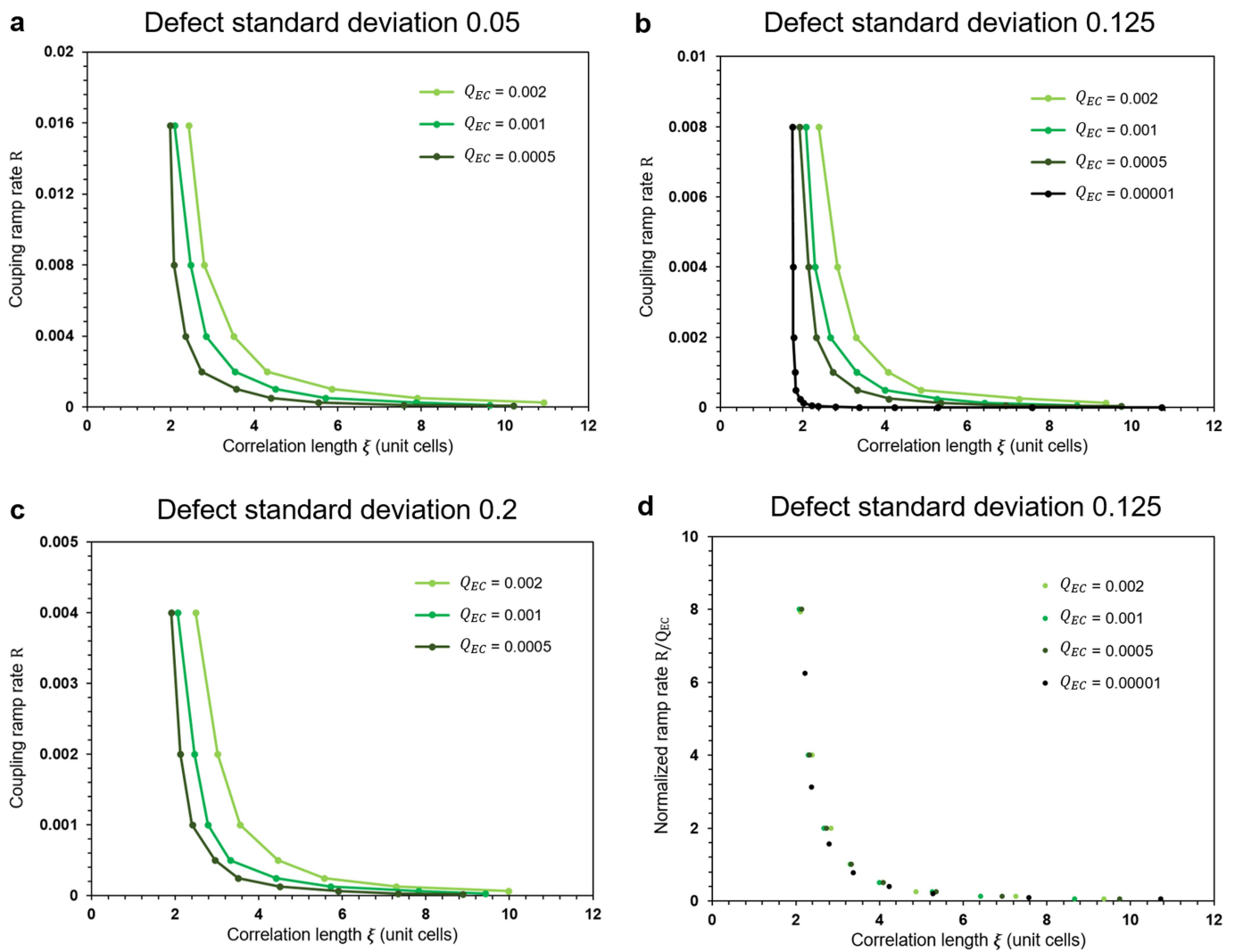
Extended Data Fig. 5 | Domain maps and correlation functions for various lithiation rates at room temperature. a–f, Representative domain maps (top row) and SEM images (bottom row) of Si microlattice samples lithiated at different rates at room temperature. Panels **c** and **d** show two samples for C/6, illustrating that nominally identical Si microlattices at the same lithiation conditions produce different domain patterns. **g,** Correlation functions at different lithiation rates with two samples per rate at room temperature. **h,** A zoomed-in plot of part of **g**, focusing on the initial decay of the correlation functions. **i,** Averaged correlation function at different lithiation rates from two samples per rate at room temperature. Data points in **g–i** are connected by straight lines.

Extended Data Fig. 6 | Influence of defect distributions and energy fluctuations in Monte Carlo simulations of domain formation dynamics. a–c, Variations in correlation length ξ with coupling ramp rate R from MC simulations with different energy fluctuations Q_{EC} (from 0.00001 to 0.002) and defect distributions h_i (from a standard deviation of 0.05 to 0.2). Data points are connected by straight lines. **d**, Relation between correlation length ξ and normalized coupling ramp rate R/Q_{EC} following the same trend for different levels of electrochemical energy fluctuations Q_{EC}.
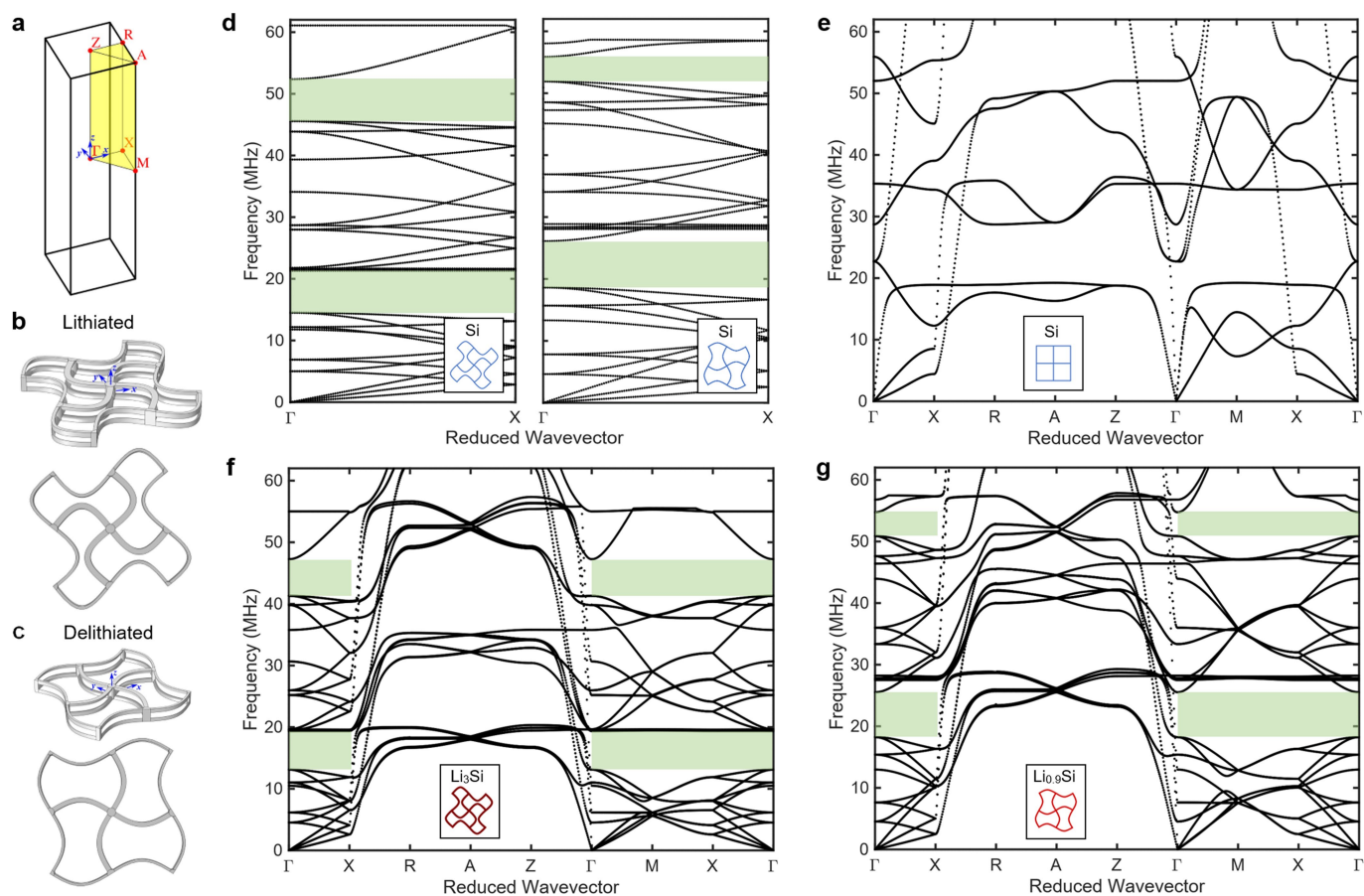
Extended Data Fig. 7 | Simulation of phononic dispersion relation for Si microlattices. a, First Brillouin zone (reciprocal space, black outline) and irreducible Brillouin zone (yellow) of the as-fabricated tetragonal lattice. The real-space coordinate system is shown in blue. **b**, Lithiated unit cell with buckled beams approximated by sinusoidal functions, resembling an 80% state of charge corresponding to a Li_3Si phase. **c**, Delithiated unit cell with a 70% Coulombic efficiency and a 0.6 V cutoff voltage corresponding to $Li_{0.9}Si$. **d**, Comparison of dispersion relations (point Γ to point X) of

buckled and partially unbuckled Si microlattices with the same curvature as the lithiated and delithiated microlattice, isolating the effects of geometric transformations from those of material property changes. **e–g**, Extended dispersion relations of as-fabricated, lithiated and delithiated Si microlattices traversing through the Brillouin zone in 3D. Insets in **d–g** represent the chemical composition and the degree of buckling for each simulation.

Extended Data Table 1 | Comparison of reported reconfiguration mechanisms

Reconfiguration mechanism	Continuous modulation	Control method	Remote deployment	Mechanical properties	Stability w/out stimuli	Response time	Minimum feature size	Number of unit cells	References
Swelling	No	Environment	No	Soft	No	5-15min	2.5μm-1mm	100	13, 14
Magnetic field	No	Magnetic field	Yes (w/ strong field)	Soft	No	0.1s	400μm	30	17
Mechanical deformation	Yes	Force or displacement	No	Soft	Discrete	10s	500μm-5cm	20	8-12
Electrochemical reactions	Yes	Voltage or current	Yes (in electrolyte)	Stiff	Yes	5-10min	1.3μm	6000 (laterally)	This work

The table compares the four reported[8–14,17] reconfiguration mechanisms for architected materials given in the leftmost column, which include the present work. A detailed description is provided in Supplementary Information section XII.